

REGULAR PAPER

Group-IV-semiconductor quantum-dots in thermal SiO₂ layer fabricated by hot-ion implantation technique: different wavelength photon emissions

To cite this article: Tomohisa Mizuno *et al* 2021 *Jpn. J. Appl. Phys.* **60** SBBK08

View the [article online](#) for updates and enhancements.



Group-IV-semiconductor quantum-dots in thermal SiO₂ layer fabricated by hot-ion implantation technique: different wavelength photon emissions

Tomohisa Mizuno^{1*}, Rikito Kanazawa¹, Kazuhiro Yamamoto¹, Kohki Murakawa¹, Kazuma Yoshimizu¹, Midori Tanaka¹, Takashi Aoki¹, and Toshiyuki Sameshima²

¹Department of Science, Kanagawa University, Hiratsuka, Kanagawa 259-1293, Japan

²Department of Engineering, Tokyo University of Agriculture and Technology, Koganei, Tokyo 184-8588, Japan

*E-mail: mizuno@kanagawa-u.ac.jp

Received October 11, 2020; revised December 11, 2020; accepted January 13, 2021; published online February 12, 2021

We experimentally studied three types of group-IV-semiconductor quantum-dots (IV-QDs) of Si-, SiC-, and C-QDs in a thermal SiO₂ layer that were fabricated using a very simple hot-ion implantation technique for Si⁺, double Si⁺/C⁺, and C⁺ into the SiO₂ layer, respectively, to realize a different wavelength photoluminescence (PL) emission from near-IR to near-UV ranges. TEM analyses newly confirmed both Si- and C-QDs with a diameter of approximately 2–4 nm in addition to SiC-QDs in SiO₂. We successfully demonstrated very strong PL emission from three IV-QDs, and the peak photon energies (E_{PH}) (peak PL-wavelength) of Si-, and SiC-, and C-QDs were approximately 1.56 eV (800 nm), 2.5 eV (500 nm), and 3.3 eV (380 nm), respectively. IV-QDs showed that the PL properties strongly depend on the hot-ion doses of Si and C atoms and the post N₂ annealing processes. Consequently, it is easy to design peak PL wavelengths by controlling the ion doses of Si⁺ and C⁺ implanted into the SiO₂ layer. © 2021 The Japan Society of Applied Physics

1. Introduction

SiC semiconductors have been widely studied to evaluate the quantum phenomena of low-dimensional SiC structures as well as for realizing SiC power devices.¹⁾ Although three-dimensional SiC is an indirect-bandgap structure, SiC can emit photoluminescent (PL) photons which are attributable to the free exciton recombination of electrons excited by photons in SiC.^{2–4)} The peak-PL photon energy (E_{PH}) of SiC is equal to the exciton energy gap (E_{GX}), which is approximately 0.1 eV lower than the bandgap energy (E_{G}).^{2–4)} Moreover, there are many diverse polytypes in SiC for which the physical properties including E_{GX} , strongly depend on the polytype,^{2,3)} so it is possible that the peak-PL wavelength (λ_{PL}) of SiC photonic devices can be controlled by the polytype. Because the E_{G} of SiC also depends on the diameter of SiC,²⁾ SiC nanostructures,²⁾—such as a porous-SiC,^{2,5–7)} 2D-SiC,^{2,8,9)} SiC-nanowires,^{2,10,11)} and SiC-dots,^{2,12,13)}—are also candidates not only for materials science, including quantum effects, but also for photonic devices with various emission wavelengths.

Using the self-clustering effects of C atoms in a Si layer via hot-C⁺ ion implantation into Si, which was evaluated by atom probe tomography (ATP),^{14–16)} SiC nano-dots (dot-diameter $\Phi \approx 2$ nm) can be easily formed in various Si crystal structures from amorphous (a-Si) to crystal Si (c-Si) by a hot-C⁺-ion implantation technique performed in the wide ranges of Si-substrate temperature T and C⁺ ion-dose D_{C} , that is, $500 \leq T \leq 1000$ °C and $5 \times 10^{12} \leq D_{\text{C}} \leq 7 \times 10^{16}$ cm⁻²,^{16–21)} to evaluate the quantum mechanical phenomena in SiC-dots as well as to realize Si-based photonic devices.^{22–24)} The self-clustering effects of ion-implanted C atoms in Si leads to the local condensation of C-atoms with the diameter of several nm in Si layer, resulting in the local formation of SiC nano-dots in Si layers.^{16,19,21)} The hot-C⁺-ion implantation process can reduce the ion-implantation-induced damage to the Si layer, which is one of the advantageous characteristics of the hot-C⁺-ion implantation process.¹⁸⁾ Moreover, the partial formation of SiC-polytypes with different E_{GX} values for cubic-(3C-SiC) and hexagonal-SiC (H-SiC) nano-dots were also

confirmed both at the oxide/Si interface and in the Si layer, using corrector-spherical aberration transmission electron microscopy (CSTEM), high-angle annular-dark-field (HAADF) scanning transmission electron microscopy (STEM), and electron diffraction (ED) patterns that were obtained by fast Fourier transform (FFT) analysis of the lattice spots of CSTEM data.¹⁶⁾ As a result, we demonstrated a broad photoluminescence (PL) spectrum with very strong emission intensity (I_{PL}) from the visible to the near-UV regions (>400 nm) even from indirect-bandgap SiC-dots, for which the I_{PL} is two orders of magnitude larger than that of 2D-Si.^{25–26)}

Because the SiC dots that have a larger E_{G} (>2.4 eV) embed in the Si layer that has a smaller E_{G} (≈ 1.1 eV),²⁷⁾ the SiC-dots in the Si layer are not quantum-dot (QD), resulting in a very small PL quantum efficiency for visible Si-based photonic devices. Thus, we experimentally realized SiC-QDs embedded in SiO₂ with a large E_{G} of 9 eV,²⁷⁾ using the simple processes of implanting double hot-Si⁺/C⁺-ion into a SiO₂ layer and post N₂ annealing at 1000 °C.²⁸⁾ HAADF-STEM observation showed that the SiC-QD diameter and density were approximately 2 nm and 1.5×10^{12} cm⁻², respectively, and the clear lattice spots of some SiC-QDs were also verified by CSTEM.²⁸⁾ Moreover, after N₂ annealing, the PL intensity of SiC-QDs rapidly increased, and as a result, we successfully confirmed that the PL quantum efficiency of SiC-QDs was approximately 2.5 times greater than that of SiC-dots in the Si layer because of the increased life time of excited electrons, which are quantum mechanically confined in SiC-QDs.²⁸⁾ Thus, the post N₂ annealing is also a key process for forming SiC-QDs. In addition, to realize different wavelength photonic devices from IR to UV ranges, QD structures with various E_{G} values, such as Si- and C-QDs as well as SiC-QDs, are also needed. Si-^{29,30)} and C-QDs³¹⁾ have been widely studied, but they have not yet been realized via the easy and simple processes of hot-ion implantation and the post N₂ annealing techniques.

In this work, we experimentally studied the group-IV-semiconductor QDs (IV-QDs) embedded in the SiO₂ layer—Si-, SiC-, and C-QDs—using very simple processes of both hot-ion implantation into the SiO₂ layer and post N₂ annealing.³²⁾ Many QD formations of Si- and C-atoms in

addition to SiC in SiO₂ layer were successfully confirmed by HAADF-STEM, and some IV-QDs also showed clear lattice spots when observed by CSTEM. We successfully demonstrated very strong PL emissions with different peak photon energies E_{PH} values from Si-QDs (near-IR) fabricated by Si⁺ hot-implantation, SiC-QDs (visible range) fabricated by double Si⁺/C⁺ hot-implantation,²⁸⁾ and C-QDs (near-UV) fabricated by C⁺ hot-implantation.

2. Experimental procedures

Using the simple fabrication processes of the hot-ion implantation into a thermal surface-SiO₂ layer (SOX) before post N₂ annealing,²⁸⁾ we realized three types of IV-QDs (Si-, SiC-, and C-QDs) in a SiO₂ layer. Figure 1 shows the fabrication steps for IV-QDs, and Table I shows the process conditions for hot-ion implantation and temperature T for each IV-QD. Figure 1(b) shows that IV-QDs were fabricated by hot-ion implantation conditions shown in Table I into the 140 nm thick SiO₂ layer (SOX) on the (100) bulk-Si substrate at T , after the SOX was formed via the dry O₂ oxidation of (100)-Si, as shown in Fig. 1(a). Table I shows that Si-, SiC- and C-QDs were fabricated by single-Si⁺, double-Si⁺/C⁺, and single-C⁺ hot-ion implantations, respectively, where $200 \leq T \leq 900$ °C, and the hot-ion dose conditions of Si⁺ (D_S) and C⁺-ion doses (D_C) were varied from 4×10^{16} to 1×10^{17} cm⁻² with the ion projection range of the middle of SiO₂ layer to realize a higher PL intensity of IV-QDs. The acceleration energies of the Si⁺ and C⁺ ions were 60 and 25 keV, respectively, for which the projection range was the middle of the SiO₂ layer. For SiC-QDs, the D_S/D_C ratio dependence of the PL properties was also studied, although our previous study²⁸⁾ showed that the optimum D_C condition for realizing higher I_{PL} of SiC-QDs was 4×10^{16} cm⁻². Figure 1(c) shows that the post N₂ annealing was carried out at an annealing temperature of $T_N = 1000$ °C for various annealing times t_N ($0 \leq t_N \leq 120$ min) to recover the crystal quality of the IV-QDs.

The PL and Raman properties of IV-QDs were measured at room temperature, at which the excitation laser energy, power, and diameter were 3.8 eV, 0.6 mW, and 1 μm, respectively. The broad-wavelength (λ_{PL}) PL spectrum from the near-UV to near-IR regions was calibrated using a standard illuminant.

3. Results and discussion

3.1. Material structures of IV-QDs

The depth profiles of implanted Si at $D_S = 6 \times 10^{16}$ cm⁻² and C-atom concentrations at $D_C = 4 \times 10^{16}$ cm⁻² in IV-QDs,

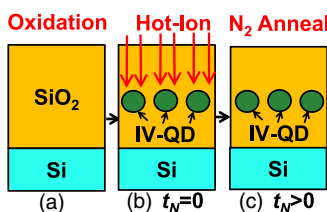


Fig. 1. (Color online) IV-QD fabrication steps via hot-ion-implantation into SiO₂ layer. After (a) dry-oxidation process of bulk-Si substrate at 1000 °C (oxide thickness $T_{\text{OX}} = 140$ nm), (b) hot-ions were implanted into SiO₂ layer at T . (c) Post N₂ annealing was carried out at T_N of 1000 °C for t_N . Process conditions for (b) are shown in Table I.

Table I. Process conditions of hot-ion temperature T and ion doses of Si (D_S) and C (D_C) for Si-, SiC- and C-QDs.

QD-type	Hot-ions	D_S ($\times 10^{16}$ cm ⁻²)	D_C ($\times 10^{16}$ cm ⁻²)	T (°C)
Si	Si ⁺	6–10		600
SiC	Si ⁺ /C ⁺	4–8	4	200–900
C	C ⁺		4–10	400–600

after N₂ annealing, were evaluated by the Si2p and C1s spectra of X-ray photoelectron spectroscopy (XPS), respectively, as shown in Fig. 2(a). The XPS accuracies for the content and depth positions were ± 1 at% and ± 2 nm, respectively, and the X-ray beam diameter was 100 μm.²¹⁾ The peak Si- and C-concentrations in the SiO₂ layer were approximately 6×10^{21} and 4×10^{21} cm⁻³, respectively. Because the Si- and C-peak concentrations are proportional to D_S and D_C , the maximum Si at $D_S = 1 \times 10^{17}$ cm⁻² and C concentrations at $D_C = 1 \times 10^{17}$ cm⁻² in this work were estimated to be the same as 1×10^{22} cm⁻³ in SiO₂. Moreover, Fig. 2(b) shows the depth profiles of the C-contents of the Si–C and C–C bonds in SiC-QDs at $T = 200$ °C (solid line) and 600 °C (dashed line), and the C-contents are nearly independent of T despite a changing 400 °C of T . Thus, Fig. 2(b) suggests that the effect of T on the C-contents of Si–C and C–C bonds is very small within a large area of 100 μm in diameter, which is similar to the results for the SiC-dots in the Si layer.²¹⁾

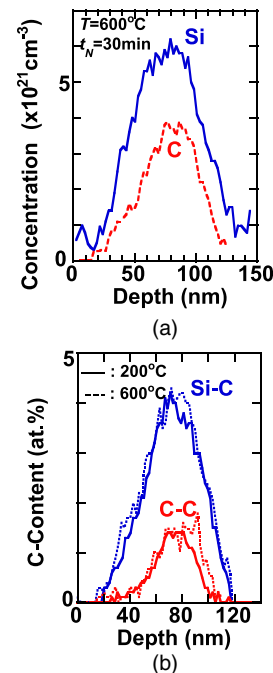


Fig. 2. (Color online) (a) Concentration depth-profiles of implanted Si (solid line) at $D_S = 6 \times 10^{16}$ cm⁻² or C (dashed line) atoms at $D_C = 4 \times 10^{16}$ cm⁻² in SiO₂ layer, which was evaluated by Si2p and C1s spectra of XPS, respectively, where $T = 600$ °C, $T_N = 1000$ °C, and $t_N = 30$ min. (b) T dependence of C-content depth profiles of Si–C (blue lines) and C–C bonds (red lines) in double Si⁺/C⁺ ion implanted SiO₂ layer at $t_N = 30$ min, where solid and dashed lines show the data at $T = 200$ °C and 600 °C, respectively. Concentration accuracy evaluated by XPS was estimated to be ± 1 at%, depth error bar was approximately ± 2 nm, and X-ray beam diameter of XPS was 100 μm. Figure 2(a) shows that the peak concentrations of Si and C atoms were approximately 6×10^{21} and 4×10^{21} cm⁻³, respectively, in the middle of SiO₂ layer. Figure 2(b) shows that the C-contents of Si–C and C–C bonds are almost independent of T .

However, the influence of T on the SiC-QD properties will be discussed in Fig. 5(c).

Next, we discuss the IV-QD structures as evaluated using electron microscopes. We experimentally confirmed many Si- and C-QDs, in addition to SiC-QDs, using HAADF-STEM observations, as shown in Figs. 3(a)–3(d). Figures 3(a) and 3(b) shows the whole SOX area and the SOX middle area of SiC-QDs, respectively, where $D_S = 6 \times 10^{16} \text{ cm}^{-2}$, $T = 600 \text{ }^\circ\text{C}$, and $t_N = 60 \text{ min}$. Si-QDs were uniformly formed in the middle SOX area with an 80 nm width of higher Si concentration region [$>2.5 \times 10^{21} \text{ cm}^{-3}$ in Fig. 2(a)], but Fig. 3(a) shows that in the surface and bottom areas of SOX with lower Si concentration, few Si-QDs could be observed. This may be attributable to the detection limitation of HAADF-STEM, that is, it is possible that the Φ of the Si-QDs in the lower Si concentration region is too small to be detected by HAADF-STEM. We also confirmed the similar depth distributions of other SiC- and C-QDs with higher dopant regions. Figures 3(c) and 3(d) also shows that other

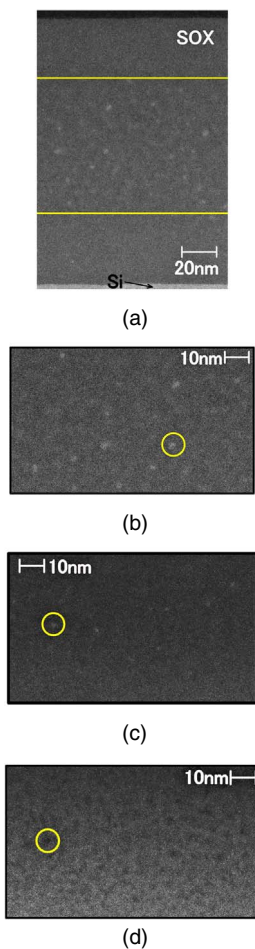


Fig. 3. (Color online) HAADF-STEM images of successful formation of many Si-QDs (encircled bright spot) in (a) whole SOX area and (b) SOX middle-area at $D_S = 6 \times 10^{16} \text{ cm}^{-2}$, $T = 600 \text{ }^\circ\text{C}$, and $t_N = 60 \text{ min}$; (c) SiC-QDs (encircled bright spot) at $D_S = 6 \times 10^{16} \text{ cm}^{-2}$, $D_C = 4 \times 10^{16} \text{ cm}^{-2}$, $T = 400 \text{ }^\circ\text{C}$, and $t_N = 60 \text{ min}$, and (d) C-QDs (encircled dark spot) at $D_C = 1 \times 10^{17} \text{ cm}^{-2}$, $T = 400 \text{ }^\circ\text{C}$, and $t_N = 30 \text{ min}$. Figure 3(a) shows that Si-QDs were uniformly formed in middle SOX area with 80 nm width in higher Si concentration region [$>2.5 \times 10^{21} \text{ cm}^{-3}$ in Fig. 2(a)], but in the surface and bottom areas of SOX with lower Si concentrations, few Si-QDs were observed. Figures 3(b)–3(d) shows that all IV-QDs were uniformly formed in middle areas of SOX layer, but their sizes vary slightly. QD surface density also depends on type of IV-QDs.

SiC- at $D_S = 6 \times 10^{16} \text{ cm}^{-2}$, $D_C = 4 \times 10^{16} \text{ cm}^{-2}$, and $T = 400 \text{ }^\circ\text{C}$ as well as C-QDs at $D_C = 1 \times 10^{17} \text{ cm}^{-2}$ and $T = 400 \text{ }^\circ\text{C}$ were uniformly formed in the middle areas of the SOX layer with higher dopant concentrations, respectively. In addition, the diameter Φ and surface density N of the IV-QDs also depend on the type of IV-QDs.

Figures 4(a) and 4(b) shows the Φ histogram of Si-QDs and the normal probability plot of Φ as those used in Fig. 3(b), respectively. The average Φ and standard deviation of Φ (σ_Φ) of Si-QDs were 2.37 and 0.28 nm, respectively. Moreover, Fig. 4(b) shows that the Φ distribution can be explained by the Gaussian function (solid line). The Φ distribution of other IV-QDs was also confirmed by the Gaussian function, which indicates that the Φ of the IV-QDs randomly fluctuates. As a result, the σ_Φ of Si-QDs ($\approx 0.28 \text{ nm}$) was much smaller than the σ_Φ of SiC- and C-QDs ($\approx 1.0 \text{ nm}$), which may be caused by the diffusion difference between Si and C atoms in SiO_2 . We will discuss the effect of N_2 annealing on the Φ of Si-QDs. Because the Si-diffusivity d_S in SiO_2 is reported to be $d_S = 1.38 \exp(-4.74 \text{ eV}/kT) \text{ cm}^2 \text{ s}^{-1}$,³³ where k denotes the Boltzmann constant and the diffusion length ($L_D \equiv 2\sqrt{d_S t_N}$)²⁷ of Si is estimated to be approximately 0.4 nm at $T_N = 1000 \text{ }^\circ\text{C}$ and $t_N = 30 \text{ min}$. Therefore, the L_D/Φ of Si-QDs is approximately 17% and is in almost the same order as σ_Φ . This L_D increase after N_2 annealing could not be observed using HAADF-STEM, because the Si-QD image at $t_N = 0$, which is considered to be small, could not be observed under the detection limitations of HAADF-STEM.²⁸

Here, we summarize the Φ and N for each type of IV-QDs, using the data in Fig. 3. Figure 5(a) shows the average Φ and N for each of the three types of IV-QDs evaluated by the HAADF-STEM data shown in Fig. 3. N was determined by

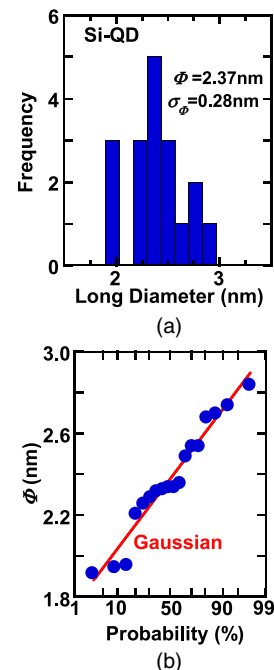


Fig. 4. (Color online) (a) Histogram of Φ of Si-QDs in 5000 nm^2 area, and (b) normal probability plot of Φ of Fig. 4(a) (circles). Process conditions of IV-QDs are the same as those in Fig. 3. Figure 4(a) shows that average Φ and σ_Φ of Si-QDs are approximately 2.37 nm and 0.28 nm, respectively. Figure 4(b) shows that Φ distribution of (a) can be explained by the Gaussian function (solid line).

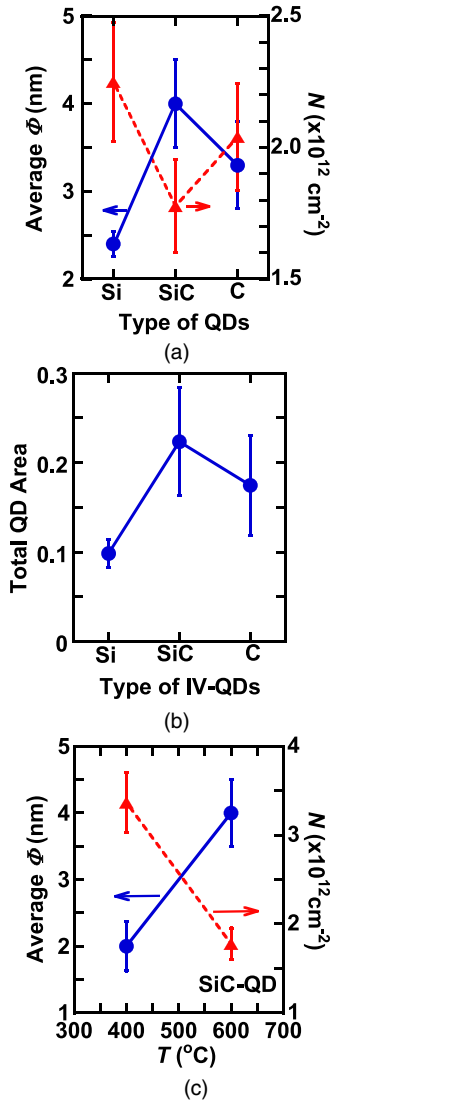


Fig. 5. (Color online) (a) Average Φ (circles) and N (triangles) and (b) total QD area S_{QD} in a unit area obtained by $S_{\text{QD}} = N\pi(\Phi/2)^2$ as a function of the type of IV-QDs of Si-, SiC-, and C-QDs, where the process conditions are the same as those in Fig. 4(c). (c) T dependence of average Φ and N in SiC-QDs, where $D_S = 6 \times 10^{16} \text{ cm}^{-2}$, $D_C = 4 \times 10^{16} \text{ cm}^{-2}$, and $t_N = 60 \text{ min}$. Figure 5(a) shows that the Φ and N strongly depend on the type of IV-QD. Φ varies from 2 to 4 nm in IV-QDs, and σ_Φ of Si-QDs, shown as an error bar, is small ($\approx 0.28 \text{ nm}$), but σ_Φ of SiC- and C-QDs is relatively large ($\approx 1.0 \text{ nm}$). N of IV-QDs was approximately $2 \times 10^{12} \text{ cm}^{-2}$ with standard deviation of approximately 20%, as shown in error bars. In addition, the N increases with decreasing Φ . Figure 5(b) shows that the S_{QD} of IV-QDs varies from approximately 0.1–0.2, and maximum variation of $\delta S_{\text{QD}}/S_{\text{QD}}$ calculated by Eq. (2) is approximately $\pm 31\%$ in SiC-QDs. Figure 5(c) shows that with decreasing T , the Φ of SiC-QDs decreases, but N increases.

the number of QDs (n) over the cross section area (S_{CS}) shown in Fig. 3, that is, $N = n/S_{\text{CS}}$. The average Φ of the IV-QDs varied from approximately 2–4 nm, and the average Φ of the Si-QDs was the smallest among the three IV-QDs. Moreover, the N of the Si-QDs was the highest of the three IV-QDs, and the IV-QD surface densities were approximately $2 \times 10^{12} \text{ cm}^{-2}$ with an error bar of 20%. The error bars of Φ and N in Fig. 5 showed the σ_Φ and the statistical deviation of N (δN), respectively, where $\delta N/N$ is given by the statistical deviation of n , that is, $\delta N/N = 1/\sqrt{n}$, assuming that n randomly fluctuates.

We discuss the total QD area (S_{QD}) of IV-QDs in the SiO_2 layer, because the PL intensity (I_{PL}) of the QDs is

proportional to S_{QD} , as shown in Eq. (1),²⁸⁾ where $S_{\text{QD}} = N\pi(\Phi/2)^2$, assuming that the QDs are spheres.

$$I_{\text{PL}} = \eta I_0 S_{\text{QD}}, \quad (1)$$

where η and I_0 denote the PL emission coefficient of IV-QDs and the excited laser flux at the surface SiO_2 . The penetration length of laser photons with 3.8 eV in the SiO_2 layer can be assumed to be infinite, because the E_G of SiO_2 (9 eV)²⁸⁾ is much higher than the laser photon energy of 3.8 eV. Moreover, the S_{QD} variation δS_{QD} can be given by the following equation:

$$\frac{\delta S_{\text{QD}}}{S_{\text{QD}}} = \sqrt{\left(\frac{2\sigma_\Phi}{\Phi}\right)^2 + \left(\frac{\delta N}{N}\right)^2} = \sqrt{\left(\frac{2\sigma_\Phi}{\Phi}\right)^2 + \left(\frac{1}{\sqrt{n}}\right)^2}. \quad (2)$$

Figure 5(b) shows the estimated S_{QD} per unit area and $\delta S_{\text{QD}}/S_{\text{QD}}$ of the three types of IV-QDs, respectively, using the data in Fig. 5(a). The S_{QD} of IV-QDs varies from approximately 0.1–0.2, which slightly depends on the type of IV-QDs. Equation (1) indicates that the S_{QD} is considered to affect the PL properties, as discussed in Sect. 3.3. The maximum $\delta S_{\text{QD}}/S_{\text{QD}}$ is approximately $\pm 31\%$ in SiC-QDs, because of the lower N of SiC-QDs shown in Fig. 5(a).

Figure 5(c) shows the T dependence of the average Φ and N in SiC-QDs, where $D_S = 6 \times 10^{16} \text{ cm}^{-2}$, $D_C = 4 \times 10^{16} \text{ cm}^{-2}$, and $t_N = 60 \text{ min}$. With increasing T , the average Φ increases, but N decreases, which is similar to the results for the SiC-dots in the Si layer.²¹⁾ Therefore, even after N_2 annealing, we confirmed the influence of T on the SiC-QD formation, which may be attributable to the SiC-QD growth by gathering small SiC-QDs during the high- T hot-ion implantation process.

Next, we discuss the crystal structures of the IV-QDs, using the lattice spots of IV-QDs evaluated by CSTEM. Figures 6(a-1), 6(b-1), 6(c-1), and 6(d) shows the CSTEM images of the cross section of Si-, H-SiC-, 3C-SiC- and C-QDs in SiO_2 (encircled areas) under the same process conditions as those in Fig. 3. All three IV-QDs show clear lattice spots, confirming that some Si- and C-QDs also consist of crystal structures. Figures 6(a-2), 6(b-2), and 6(c-2) shows the ED patterns of [111]Si with lattice spaces $d = 0.314 \text{ nm}$, [10 $\bar{1}$ 3] H-SiC with $d = 0.237 \text{ nm}$, and (111) 3C-SiC with $d = 0.251 \text{ nm}$, as evaluated by FFT analysis of the lattice spots of Figs. 6(a-1), 6(b-1), and 6(c-1), respectively. As a result, it was found that SiC-QDs also consist of 3C- and H-SiC polytypes, although it has already been confirmed^{16,19,21)} that SiC-dots in the Si layer consist of 3C- and H-SiC polytypes. In contrast, the lattice distance of the C-atoms in Fig. 6(d) was approximately 0.36 nm, which is nearly equal to the layer distance of graphite ($\approx 0.335 \text{ nm}$).³⁴⁾ Thus, some C-QDs consist of nano-graphite with a diameter of approximately 2 nm, as indicated by the G- and D-bands of the UV-Raman spectroscopy shown in Fig. 7(b). However, all IV-QDs, as confirmed by the HAADF-STEM images in Figs. 3(a)–3(c), showed no clear lattice spots. For example, only 1/4 of the Si-QDs, confirmed by HAADF-STEM, shows clear lattice images via CSTEM. Therefore, the crystal quality of some IV-QDs is poor, which suggests that some part of C-QDs consist of a-C. Consequently, IV-QDs consist of both amorphous and crystal structures.

As an example of a Si-QD for which the crystal structure is clear, we estimate the Si atom number of Si-QDs observed by

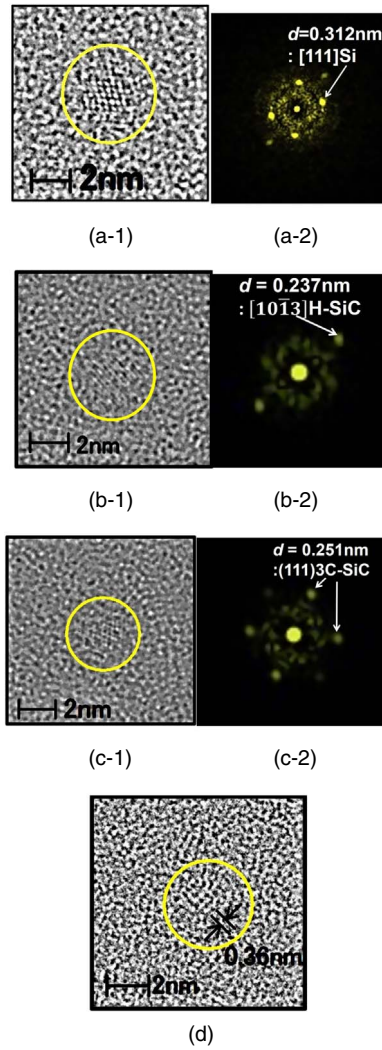


Fig. 6. (Color online) CSTEM lattice images of cross sections of (a-1) Si-QD, (b-1) H-SiC-QD, (c-1) 3C-SiC-QD, (d) C-QD, and ED-patterns of (a-2) [111]Si-QD, (b-2) H-SiC-QD, and (c-2) 3C-SiC-QD evaluated by FFT analyses of (a-1), (b-1), and (c-1), in which the process conditions are the same as Fig. 3. Lattice spaces of 0.237 nm of (b-2) and 0.251 nm of (c-2) indicate that polytypes of SiC-QD of (b-1) and (c-1) are [10 $\bar{1}$ 3] H-SiC and (111) 3C-SiC, respectively. Lattice distance of C-QD in (d) was approximately 0.36 nm, which is nearly equal to the layer distance of graphite (≈ 0.335 nm).³⁴⁾

HAADF-STEM data in Figs. 5(a)–5(b), compared with that via the XPS data shown in Fig. 2(a). First, we estimate the Si atom number of the Si-QDs N_{QD} using Eq. (3).

$$N_{\text{QD}} = N_{\text{Si}} S_{\text{QD}} W, \quad (3)$$

where N_{Si} is the Si volume density ($\equiv 5 \times 10^{22} \text{ cm}^{-3}$),²⁷⁾ $S_{\text{QD}} \approx 0.1$ in Fig. 5(b), and W denotes the depth width of the Si-QD formation area (≈ 80 nm) shown in Fig. 3(a), resulting in $N_{\text{SD}} \approx 4 \times 10^{16} \text{ cm}^{-2}$.

In contrast, the Si atom number via the XPS data in Fig. 2(a); N_{XPS} was obtained by integrating the depth profile of the Si atom profile with more than $2.5 \times 10^{21} \text{ cm}^{-3}$ of the Si-QD formation area shown in Fig. 3(a), resulting in $N_{\text{XPS}} \approx 3.6 \times 10^{16} \pm 0.5 \times 10^{16} \text{ cm}^{-2}$. Thus, $N_{\text{SD}} \approx N_{\text{XPS}}$ within an XPS accuracy of 1 at%. Consequently, we confirmed that approximately 100% of the Si atoms evaluated by XPS data form Si-QDs, as observed by HAADF-STEM in Fig. 3(a).

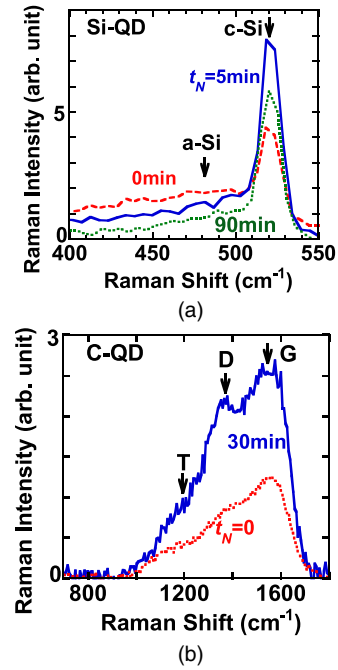


Fig. 7. (Color online) t_N dependence of UV-Raman spectrum of (a) Si-QD at $D_S = 6 \times 10^{16} \text{ cm}^{-2}$, and (b) C-QD at $D_C = 1 \times 10^{17} \text{ cm}^{-2}$, where $T = 600^\circ \text{C}$. Arrows in (a) show the peak Raman positions of c-Si (520 cm^{-1}), including Raman intensity from Si-substrate under SOX layer and a-Si in Si-QDs (480 cm^{-1}). After N_2 annealing, peak Raman intensity of c-Si increases, but the peak Raman intensity of a-Si decreases. Arrows in (b) show T (a-C), D, and G bands of graphite, and after N_2 annealing, all peak-Raman intensities of graphite also increase.

3.2. UV-Raman properties of IV-QDs

In this subsection, we discuss the material properties of the IV-QDs evaluated by UV-Raman spectroscopy. Figures 7(a) and 7(b) shows the t_N dependence of the UV-Raman spectrum of Si- at $D_S = 6 \times 10^{16} \text{ cm}^{-2}$ and C-QDs at $D_C = 1 \times 10^{17} \text{ cm}^{-2}$, respectively, where $T = 600^\circ \text{C}$. The arrows in Fig. 7(a) show the peak Raman shifts of c-Si (520 cm^{-1}), including the Raman intensity I_{R0} from the Si-substrate under the SOX layer, in addition to a-Si in Si-QDs (480 cm^{-1}). The peak Raman intensity of c-Si increases and the a-Si Raman peak decreases after N_2 annealing, where the measured c-Si Raman intensity minus I_{R0} ($\equiv \Delta I_R$) shows the net Si-Raman intensity of Si-QDs in SiO_2 . Thus, the crystal quality of Si-QDs can be improved via N_2 annealing. Moreover, the arrows in Fig. 7(b) show the T-, D-, and G-bands of C–C vibrations in C-QDs. After N_2 annealing, the peak Raman intensities of the G- and D-bands increased, but the N_2 annealing effect on the T-band intensity was small. Thus, the graphite component of C-QDs, which was already confirmed via CSTEM, as shown in Fig. 6(c), also increases after N_2 annealing. Our previous work²⁸⁾ on the t_N dependence of UV-Raman analysis for SiC-QDs also demonstrated that the peak-Raman intensities of the D-, T-, and TO-modes of Si–C vibration increase after a brief N_2 annealing, which leads to the improvement of the quality of the SiC-QDs.

Figure 8(a) shows the UV-Raman spectra of SiC-QDs as a function of the D_S/D_C dose ratio at a fixed D_C of $4 \times 10^{16} \text{ cm}^{-2}$, where $T = 200^\circ \text{C}$ and $t_N = 0$. The arrows in Fig. 8(a) show the G-, D-, and T-bands, which are attributable to the separated C atom areas in SiO_2 ,²⁸⁾ and the TO mode of the Si–C vibration. The Raman spectrum line shape

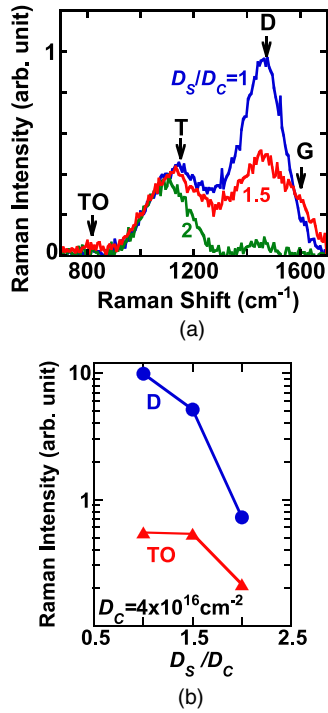


Fig. 8. (Color online) D_S/D_C -ratio dependence of (a) UV-Raman spectrum and (b) peak TO- and D-band intensities of SiC-QD, where $D_C = 4 \times 10^{16} \text{ cm}^{-2}$, $T = 200 \text{ }^\circ\text{C}$, and $t_N = 0$. Arrows in Fig. 8(a) show G, D and T bands of C–C vibrations, and TO mode of Si–C vibration. Figure 8(a) shows that Raman spectrum line shape strongly depends on D_S/D_C . Figure 8(b) shows that peak Raman intensities of D- and TO-bands increase with decreasing D_S/D_C .

strongly depends on D_S/D_C even at the same D_C . The G band can be observed at $D_S/D_C \leq 1.5$. Moreover, Fig. 8(b) shows the peak Raman intensities of the D- and TO-bands versus D_S/D_C at the same data used in Fig. 8(a). The D-band intensity increases with decreasing D_S/D_C , which suggests that the separated C atoms in SiO_2 increase at low D_S conditions. The TO intensity is reduced only at $D_S/D_C = 2$. Thus, the Si–C bond formation shown by the TO-mode increases with decreasing D_S , so this study indicates that $D_S/D_C \leq 1.5$ is optimum for forming SiC in this study.

3.3. PL properties

3.3.1. QD type dependence. In this subsection, we discuss the PL properties as a function of the type of IV-QDs. Figure 9(a) shows the PL spectrum comparison among three types of IV-QDs: Si-QDs (solid line: $D_S = 6 \times 10^{16} \text{ cm}^{-2}$, $T = 600 \text{ }^\circ\text{C}$, $t_N = 1.5 \text{ h}$), SiC-QDs (dashed line: $D_S = 6 \times 10^{16} \text{ cm}^{-2}$, $D_C = 4 \times 10^{16} \text{ cm}^{-2}$, $T = 200 \text{ }^\circ\text{C}$, $t_N = 30 \text{ min}$), and C-QDs (dotted line: $D_C = 1 \times 10^{17} \text{ cm}^{-2}$, $T = 600 \text{ }^\circ\text{C}$, $t_N = 30 \text{ min}$) after N_2 annealing, in which the PL intensity of SiC-DQ is reduced to 1/3 of measured PL data. The lower and upper axes show the PL photon energy and wavelength λ_{PL} , respectively. We experimentally demonstrated the PL emissions from three types of IV-QDs with different peak-PL energy E_{PH} (peak- λ_{PL}) emissions from Si-QDs (near-IR), SiC-QDs (visible region), and C-QDs (near-UV). Thus, the PL spectrum line shape and I_{PL} strongly depend on the type of IV-QDs, and the E_{PH} (peak- λ_{PL}) of Si-, and SiC-, and C-QDs were approximately 1.56 eV (800 nm), 2.42 eV (500 nm), and 3.28 eV (380 nm), respectively. The I_{PL} of the SiC-QDs was the largest and was approximately 2.6 and 6.6 times greater than that of Si- and C-QDs, respectively. Moreover, the Si-QDs showed a very sharp PL spectrum with a FWHM of 0.36 eV, compared with the broad FWHM of SiC- (0.85 eV) and

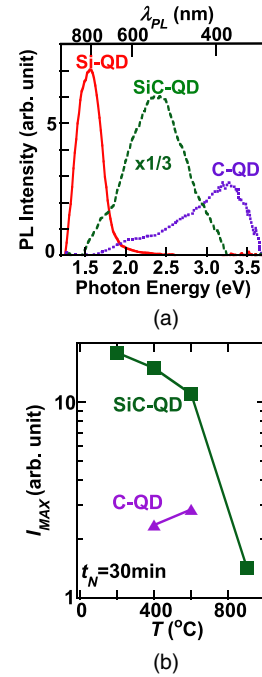


Fig. 9. (Color online) (a) PL spectrum comparison among three IV-QDs of Si-QD (solid line: $D_S = 6 \times 10^{16} \text{ cm}^{-2}$, $T = 600 \text{ }^\circ\text{C}$, $t_N = 1.5 \text{ h}$), SiC-QD (dashed line: $D_S = 6 \times 10^{16} \text{ cm}^{-2}$, $D_C = 4 \times 10^{16} \text{ cm}^{-2}$, $T = 200 \text{ }^\circ\text{C}$, $t_N = 30 \text{ min}$), and C-QD (dotted line: $D_C = 1 \times 10^{17} \text{ cm}^{-2}$, $T = 600 \text{ }^\circ\text{C}$, $t_N = 30 \text{ min}$). Lower and upper axes show the PL photon energy and wavelength, respectively. The PL intensity of SiC-DQ is reduced to 1/3 of measured PL data. PL spectrum strongly depends on type of IV-QDs, and very different E_{PH} (peak- λ_{PL}) values were realized among three IV-QDs. E_{PH} (peak- λ_{PL}) of Si-, and SiC-, and C-QDs were approximately 1.56 eV (800 nm), 2.42 eV (500 nm), and 3.28 eV (380 nm), respectively. (b) T dependence of I_{MAX} of SiC-QDs (squares) and C-QDs (triangles) under the same ion dose conditions as those shown in Fig. 9(a). Figure 9(b) shows that optimum T conditions for increasing I_{MAX} of SiC- and C-QDs are $200 \text{ }^\circ\text{C}$ and $600 \text{ }^\circ\text{C}$ after N_2 annealing, respectively.

C-QDs (0.89 eV). The broad PL spectrum of SiC-QDs can be explained by the PL components of cubic and hexagonal SiC-polytypes with different E_{GX} , as discussed in Fig. 15. Consequently, it is easy for IV-QDs to control PL emission wavelength from near-IR to near-UV by changing the type of atoms implanted into the SiO_2 layer. The PL emission mechanisms for SiC- and Si-QDs are attributable to the sum of the emissions from various SiC polytypes as shown in Fig. 15, and the quantum-mechanically induced E_G -expansion of Si-QDs which are indicated in Fig. 11(b), respectively. However, the physical mechanism for C-QD emission is not currently understood, but it may be caused by the photon emissions from a-C and nano-graphite.^{31,34} Moreover, Fig. 9(b) shows the T dependence of the maximum I_{PL} (I_{MAX}) of SiC-QDs (squares) and C-QDs (triangles) at the same ion dose conditions in Fig. 9(a). The I_{MAX} of SiC-QDs drastically increases with decreasing T , but the I_{MAX} of C-QDs slightly increases with increasing T . As a result, the optimum T conditions for realizing the strongest I_{MAX} of SiC- and C-QDs are $200 \text{ }^\circ\text{C}$ and $600 \text{ }^\circ\text{C}$, respectively. This T dependence of SiC-QDs could be attributable to the N increase in the SiC-QDs at lower T conditions.²⁸ Therefore, we will discuss the PL data of SiC- and C-QDs under the optimum T conditions shown in Fig. 9(b).

Next, we address the effect of N_2 annealing on the PL properties of IV-QDs. Figures 10(a)–10(c) shows the t_N dependence of the PL spectra of the Si-, SiC-, and C-QDs,

respectively, where the process conditions of IV-QDs are the same as those in Fig. 9. The PL spectrum line shape of each IV-QD after N_2 annealing is mostly independent of t_N . However, the I_{PL} drastically increases with increasing t_N , but the I_{PL} increase factors of N_2 annealing are also affected by the type of IV-QDs. The I_{PL} of the three IV-QDs rapidly increases after short N_2 annealing, and in particular, the t_N dependence of the I_{PL} of Si-QDs continues to grow larger with increasing t_N even for long t_N value.

We summarize the t_N dependence of the PL properties of IV-QDs. Figures 11(a) and 11(b) shows the t_N dependence of the I_{MAX} and E_{PH} (peak- λ_{PL}) under the same process conditions in Fig. 9, respectively, where circles, squares, and triangles show the data of Si-, SiC-, and C-QD, respectively, and the right vertical axis in Fig. 11(b) shows the peak PL wavelength (peak- λ_{PL}). The rhombi in Fig. 11(a) show the data of SiC dots in the Si layer at $D_C = 4 \times 10^{16} \text{ cm}^{-2}$ and $T = 600^\circ\text{C}$. Both the I_{MAX} and

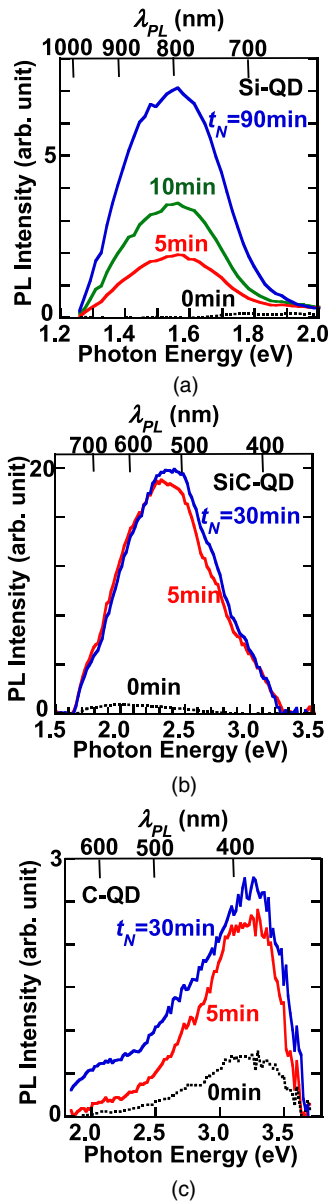


Fig. 10. (Color online) t_N dependence of PL spectrum of (a) Si-, (b) SiC-, and (c) C-QDs, where process conditions of IV-QDs are the same as those seen in Fig. 9. PL spectrum line shape of each IV-QD is nearly independent of t_N , but PL intensity of each QDs increases with increasing t_N .

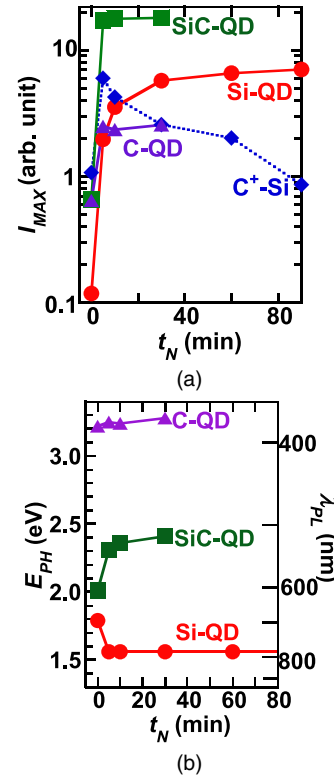


Fig. 11. (Color online) t_N dependence of (a) I_{MAX} , and (b) E_{PH} (left vertical-axis) and peak- λ_{PL} (right vertical-axis) at the same data of Fig. 9 [Si-QD (circles), SiC-QD (squares), and C-QD (triangles)]. Rhombi in Fig. 11(a) show the data of SiC dots in c-Si layer at $D_C = 4 \times 10^{16} \text{ cm}^{-2}$ and $T = 600^\circ\text{C}$. I_{MAX} of three IV-QDs rapidly increases after a brief N_2 annealing and continues increasing with increasing t_N . However, only SiC dots in c-Si layer decrease with increasing t_N under $t_N \geq 5$ min. As shown in Fig. 11(b), only SiC-QDs shows the rapid increase of E_{PH} after a brief N_2 annealing, because 3C-SiC, which have an $E_{GX} = 2.39$ eV, was formed. However, the E_{PH} of other IV-QDs is nearly independent of t_N . Figures 11(a) and 11(b) show that both the I_{MAX} and E_{PH} (peak- λ_{PL}) of IV-QDs strongly depend on the type of IV-QDs. The I_{MAX} of SiC-QDs is approximately 2.6 and 6.6 times greater than that of Si- and C-QDs, respectively. Consequently, the E_{PH} of IV-QDs varies from 1.56 to 3.28 eV, that is, peak- λ_{PL} of IV-QDs varies from 380 to 800 nm.

E_{PH} (peak- λ_{PL}) of IV-QDs strongly depend on the type of IV-QDs. The I_{MAX} of IV-QDs rapidly increased after a brief N_2 annealing, which could be attributable to the improved crystal quality of IV-QDs, as shown by the Raman data of IV-QDs in Figs. 7(a) and 7(b). The maximum I_{MAX} enhancement factors of Si-, SiC-, and C-QDs, compared to I_{MAX} at $t_N = 0$, reached approximately 59, 23, and 3.3, respectively, which indicates that post N_2 annealing is also a key process in realizing a higher I_{PL} . Thus, the I_{MAX} enhancement factor of Si-QDs is at its maximum in the three IV-QDs. In addition, even during high- T_N annealing, the I_{MAX} of IV-QDs continues to increase with increasing t_N . However, Fig. 11(a) shows that SiC-dots in the Si layer show a drastic decrease in I_{MAX} with increasing t_N , that is, $I_{MAX}(t_N) \propto \exp(-t_N/t_D)$, where t_D is a decay scaling time of approximately 21 min.²¹⁾ Thus, the SiC-dot structures in the Si layer are thermally unstable at high T_N conditions, which may be caused by the decomposition of SiC during high- T_N annealing.²¹⁾ Consequently, IV-QD structures have thermal stability even at a higher T_N , which is an advantageous characteristic of IV-QDs in the SiO_2 layer.

Figure 11(b) shows that different peak- λ_{PL} values for a near-IR of 800 nm to a near-UV of 380 nm can be obtained

only by changing the type of IV-QDs. Moreover, only SiC-QDs showed strong t_N dependence on E_{PH} , because the E_{PH} increase from 2.0 eV of Si-C alloy at $t_N = 0$ to 2.3 eV at $t_N = 5$ min could be attributable to the 3C-SiC ($E_{GX} = 2.39$ eV) QD-formation that occurs by binding the Si-C atoms during high- T_N annealing for $t_N = 5$ min.²⁸⁾ Because Fig. 5(a) shows that the Φ of SiC-QDs is approximately 4 nm and relatively large, and in addition, the quantum-mechanics effects on E_G expansion ($E_G \propto \Phi^{-2}$) in SiC-QDs occurs in $\Phi < 3$ nm,²⁾ the quantum-mechanical effects on E_G expansion of SiC-QDs in this study was very small. On the other hand, Fig. 11(b) shows that the E_{PH} of Si-QDs with $\Phi \approx 2.5$ nm [as shown in Fig. 5(a)] was 1.56 eV, which is nearly equal to the reported experimental results reached in E_G via quantum E_G -expansion of Si-QDs at $\Phi \approx 3$ nm.³⁵⁾ In addition, considering the long tailing of the PL spectrum of Si-QDs at the half-width-tenth-maximum (HWTM), shown in Figs. 9 and 10(a), the HWTM of E_{PH} in Si-QDs (δE_{PH}) was approximately 0.28 eV. Assuming that the δE_{PH} is attributable to the quantum E_G -expansion of $E_G \propto \Phi^{-2}$, this δE_{PH} is caused by the σ_Φ shown in Fig. 5(a), so $\delta E_{PH}/E_{PH}$ can be given by Eq. (4)

$$\frac{\delta E_{PH}}{E_{PH}} = 2 \frac{\sigma_\Phi}{\Phi}. \quad (4)$$

Therefore, the experimental $\delta E_{PH}/E_{PH}$ seen in Fig. 9 was approximately 0.18, and the $\delta E_{PH}/E_{PH}$ obtained by substituting the experimental σ_Φ/Φ of 0.12 in Fig. 5(a) into Eq. (4) was 0.24, which is neatly equal to the experimental $\delta E_{PH}/E_{PH}$. As a result, Eq. (4) is nearly valid in Si-QDs, so the HWTM of the PL spectrum in Si-QDs is also attributable to the statistical variation of the Si-QD diameter. Thus, for Si-QDs, we experimentally confirmed the quantum E_G -expansion of Si-QDs in this study.

We summarize the QD type dependence of the PL properties. Figure 12(a) shows the QD type dependence of I_{MAX} (circles) and E_{PH} (squares) for the same data as that used in Figs. 9 and 11. The I_{MAX} of SiC-QDs is approximately 2.6 and 6.6 times greater than that of the Si- and C-QDs, respectively. Moreover, the E_{PH} of IV-QDs can be controlled by the type of IV-QDs in the range of $1.5 < E_{PH} < 3.3$ eV ($380 < \text{peak-}\lambda_{PL} < 800$ nm). Assuming that the PL emission coefficient η of Eq. (1) is independent of the type of IV-QDs, the universal $I_{MAX} \propto S_{QD}$ of Eq. (1) should be valid in the three IV-QDs. Figure 12(b) shows the I_{MAX} as a function of the S_{QD} [Fig. 5(b)] of Si- (circle), SiC- (square), and C-QDs (triangle). We verified that the I_{MAX} of Si- and SiC-QDs obeyed Eq. (1) [dashed line in Fig. 12(b)], which indicates that the η of Si-QDs is almost equal to that of SiC-QDs. However, the I_{MAX} of the C-QDs deviates from the dashed line in Eq. (1). We estimate the η of QDs by $\eta = I_{MAX}/I_0 S_{QD}$ of Eq. (1), where the η deviation ($\delta\eta$) can be expressed by $\delta\eta/\eta = \delta S_{QD}/S_{QD}$ and $\delta S_{QD}/S_{QD}$ is given by Eq. (2). Figure 12(c) shows the η of the IV-QDs as a function of the type of IV-QD. The η of the Si-QDs is equal to that of the SiC-QDs, as shown in Fig. 12(b), but the η of the C-QDs is approximately 1/4 of those of the Si- and SiC-QDs. The physical mechanism for the low η in the C-QDs is not currently understood, but it is possible that the fabrication conditions for C-QDs, such as the T of hot-ion implantation, were not optimized in this work, resulting in poor quality C-QDs.

3.3.2. Process dependence. Figure 13(a) shows the ion dose dependence of I_{MAX} and E_{PH} of Si- (circles) and C-QDs (triangles) after N_2 annealing, respectively, in which

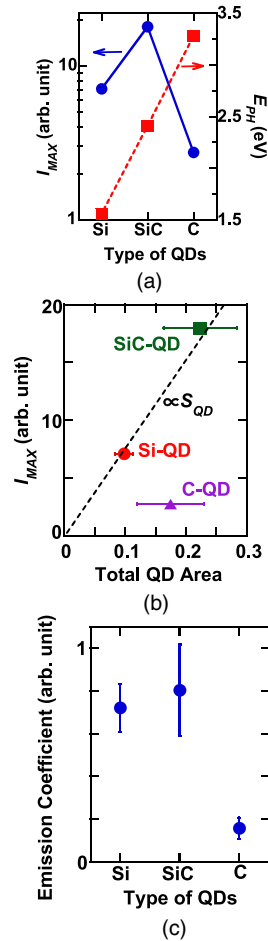


Fig. 12. (Color online) (a) Summary of QD type dependence of I_{MAX} (circles) and E_{PH} (squares) using the same data in Fig. 9, (b) total QD area dependence of I_{MAX} , and (c) QD type dependence of η (circles) calculated by substituting I_{MAX} and S_{QD} into Eq. (1) using the same data in Fig. 12(a). Circle, square, and triangle in Fig. 12(b) show the data for the Si-, SiC-, and C-QDs, respectively. Dashed line in Fig. 12(b) shows the $I_{MAX} \propto S_{QD}$ relationship of Eq. (1), and the data for Si- and SiC-QDs obey Eq. (1) of $I_{MAX} \propto S_{QD}$, but the I_{MAX} of C-QDs deviates from the dashed line of Eq. (1). Figure 12(c) shows that the η of Si-QDs is equal to that of SiC-QDs, but the η of C-QDs is approximately 1/4 of those of Si- and SiC-QDs.

$T = 600$ °C. With an increasing ion dose, the I_{MAX} of Si-QDs decreases, but the I_{MAX} of C-QDs increases. The E_{PH} of Si-QDs is nearly independent of D_S , but the E_{PH} of the C-QDs increases with increasing D_C . It has already been reported³⁶⁾ that an integrated Raman intensity ratio—G-band to D-band of C-C vibration (S_G/S_D)—shown in Eq. (5) is an indicator of the quality of the graphite. In the following equation

$$\frac{S_G}{S_D} = \frac{\int I_G(\omega) d\omega}{\int I_D(\omega) d\omega}, \quad (5)$$

where ω is the wavenumber, and I_G and I_D denote the fitting Raman spectra of the G- and D-bands for the measured data, respectively. Figure 13(b) shows the ion dose dependence of the peak Si-Raman intensity I_R (circles) of c-Si (520 cm^{-1}) of Si-QDs and the S_G/S_D (triangles) of C-QDs, when the process conditions are the same as those used in Fig. 13(a). The I_R of Si-QDs increases with decreasing D_S , which indicates that the Si-QD quality improved at a lower D_S , because of the ion-

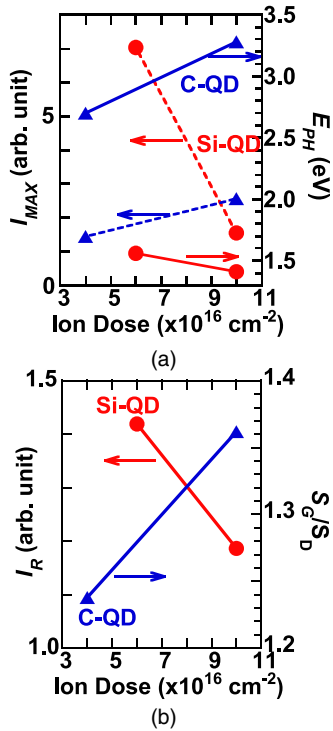


Fig. 13. (Color online) Ion dose dependence of (a) I_{MAX} (dashed lines) and E_{PH} (solid lines) of Si-QD (circles) and C-QD (triangles), and (b) Raman intensity I_R at 520 cm^{-1} of Si-QDs (circles) and DG-band-integrated intensity ratio S_G/S_D of C-QDs (triangles) of Eq. (5), where $T = 600 \text{ }^\circ\text{C}$ and $t_N = 30 \text{ min}$. Figure 13(a) shows that the I_{MAX} of Si-QDs increases with decreasing D_S , but the I_{MAX} of C-QDs increases with increasing D_C . The E_{PH} of Si-QDs slightly increases with decreasing D_S , but the E_{PH} of C-QDs increases with increasing D_C . Figure 13(b) shows that I_R of Si-QDs increases with decreasing D_S , but the S_G/S_D of C-QDs increases with increasing D_C .

implantation damage reduction of Si-QDs at a lower D_S . In contrast, the S_G/S_D of C-QDs increases with increasing D_C , which suggests that the graphite quality improved at a higher D_C . Consequently, the I_{MAX} and E_{PH} of Si- and C-QDs strongly depend on the ion dose, which is attributable to the ion dose dependence of the QD crystal quality.

Next, the PL spectrum of SiC-QDs strongly depends on the D_S/D_C ratio even at a fixed D_C condition of $4 \times 10^{16} \text{ cm}^{-2}$, as shown in Fig. 14(a), where $T = 200 \text{ }^\circ\text{C}$ and $t_N = 5 \text{ min}$. The arrows in Fig. 14(a) show the E_{PH} -positions. Figure 14(a) shows that the PL spectrum line shape strongly depends on the D_S/D_C . The I_{PL} at $D_S/D_C = 1.5$ is almost the same as that at $D_S/D_C = 1$, and the I_{PL} drastically decreases at $D_S/D_C = 2$, but the E_{PH} increases with decreasing D_S/D_C . In summary, Fig. 14(b) shows the I_{MAX} and E_{PH} of SiC-QDs as a function of D_S/D_C under the same process conditions as those used in Fig. 14(a). With decreasing D_S/D_C , both the I_{MAX} and E_{PH} of the SiC-QDs continue to increase even at the same D_C . In other words, after N_2 annealing, the I_{MAX} of the SiC-QDs is nearly constant under $D_S/D_C \leq 1.5$, and rapidly decreases at $D_S/D_C = 2$, because of the reduced Si-C bonding shown as the TO intensity reduction in Fig. 8(b). Thus, the condition of $D_S/D_C \leq 1.5$ is optimum for realizing a higher I_{PL} in SiC-QDs. In addition, the large D_S/D_C dependence of E_{PH} indicates that the peak- λ_{PL} of SiC-QDs can be controlled by D_S/D_C .

Our previous work¹⁹⁾ showed that the broad PL spectrum of SiC-dots in a-Si can be explained by five PL components of different SiC-polytypes of cubic- and hexagonal-SiC as

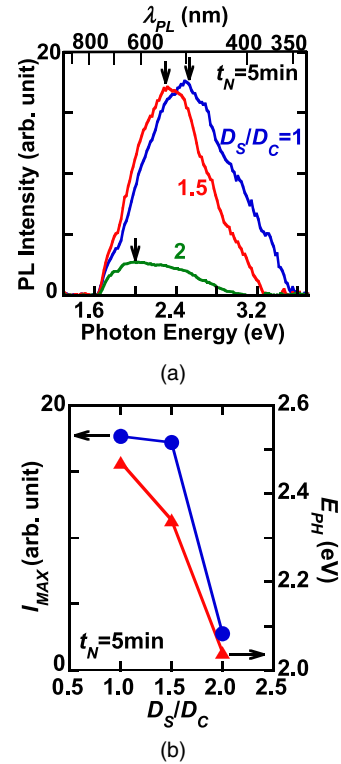


Fig. 14. (Color online) D_S/D_C -ratio dependence of (a) PL spectrum and (b) I_{MAX} (circles) and E_{PH} (triangles) after N_2 annealing ($t_N = 5 \text{ min}$), where D_C is fixed to $4 \times 10^{16} \text{ cm}^{-2}$ and $T = 200 \text{ }^\circ\text{C}$. Arrows in (a) show E_{PH} -positions. Figure 14(a) shows that the PL spectrum of SiC-QDs strongly depends on D_S/D_C , that is, D_S at a fixed D_C . Figure 14(b) shows that the I_{MAX} of SiC-QDs drastically decreases at $D_S/D_C = 2$, and in addition, the E_{PH} also decreases with increasing D_S/D_C .

well as an additional Si-C alloy, whereas the broad PL spectrum of SiC-dots in c-Si is attributable to the sum of only four PL components of different SiC-polytypes, which excludes the Si-C alloy.²¹⁾ This Si-C alloy component, which has an $E_{\text{GX}} < 2.39 \text{ eV}$ (3C-SiC), suggests an imperfect SiC structure in SiO_2 .¹⁹⁾ Actually, Fig. 15(a) shows that the measured PL spectrum at $D_S/D_C = 1$ (bold line) can be well fitted via five PL component fitting [Gaussian curve (dashed lines)] even in SiC-QDs, where D_C is fixed to $4 \times 10^{16} \text{ cm}^{-2}$, $t_N = 5 \text{ min}$, and $T = 200 \text{ }^\circ\text{C}$. Thus, the PL spectrum of SiC-QDs in SiO_2 can be also explained by the sum of the PL emissions from four different SiC-polytypes: 3C-SiC, which has an E_{GX} of 2.39 eV (3C: red); 8H-SiC, which has an E_{GX} of 2.73 eV (8H: green); 6H-SiC, which has an E_{GX} of 3.05 eV (6H: blue); 4H-SiC, which has an E_{GX} of 3.32 eV (4H: purple); and an additional one-component of Si-C alloy (SC: brown), which has an E_{GX} of lower than 2 eV.¹⁹⁾ We can estimate the total photon emission number from each PL component, which is an indicator for each polytype ratio for the SiC and Si-C alloy.¹⁹⁾ The integrated PL component ratio P_I of the one PL component I_I to the total I_{PL} emission (subscript I is from SC to 4H), as shown in Fig. 15(a), was calculated using Eq. (6).¹⁹⁾

$$P_I = \int I_I(E) dE / \int I_{\text{PL}}(E) dE, \quad (6)$$

where E is the photon energy. Figure 15(b) shows the integrated intensity ratio of the five PL components¹⁹⁾ of SiC-QDs as a function of D_S/D_C , and the P_I ratio strongly

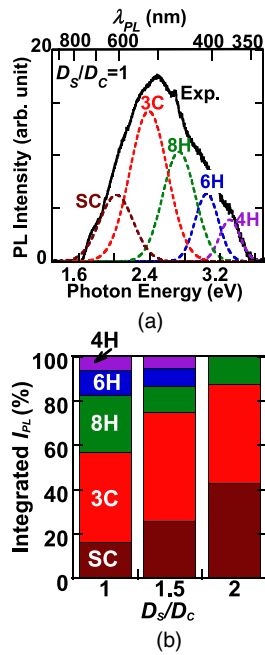


Fig. 15. (Color online) (a) Five PL component fittings [Gaussian curve (dashed lines)] for measured PL spectrum at $D_S/D_C = 1$ (solid line) and (b) integrated PL intensity ratios of five PL components of SiC-QD calculated by Eq. (6) as a function of D_S/D_C , where D_C is fixed at $4 \times 10^{16} \text{ cm}^{-2}$, $t_N = 5 \text{ min}$, and $T = 200 \text{ }^\circ\text{C}$. Figure 15(a) shows that the PL spectrum of SiC-QDs can also be explained by the sum of five PL components¹⁹⁾ from four different SiC-polytypes of 3C-SiC with E_{GX} of 2.39 eV (I_{3C} : red), 8H-SiC with E_{GX} of 2.73 eV (I_{8H} : green), 6H-SiC with E_{GX} of 3.05 eV (I_{6H} : blue), 4H-SiC with E_{GX} of 3.32 eV (I_{4H} : purple), and an additional one-component of Si-C alloy I_{SC} (brown) with lower E_G of 2 eV. Figure 15(b) shows that five PL component ratio of Eq. (6) strongly depends on D_S/D_C . Hexagonal PL component ratio increases with decreasing D_S/D_C , but the 3C-SiC PL component is almost independent of D_S/D_C .

depends on D_S/D_C . The 3C-SiC PL component ratio of approximately 44% is nearly independent of D_S/D_C . However, with decreasing D_S/D_C , the hexagonal-SiC PL component ratio increases, and the SC component rapidly decreases. Thus, the SC component indicates that the imperfect SiC formation of the Si-C alloy in SiO_2 increases with increasing D_S/D_C . Consequently, even at the same D_C , the SiC-QD formation is strongly affected by D_S , and the H-SiC polytype ratio increases with an increasing D_C ratio. These results regarding the D_S/D_C dependence of PL components can indicate that the peak- λ_{PL} (E_{PH}) can also be controlled by D_S/D_C , as shown in Figs. 14(b) and 15(b).

According to the different PL peak wavelengths versus the type of IV-QDs shown in Figs. 9, 11(b), 12(a), and 14(b), the peak- λ_{PL} of IV-QDs in SiO_2 can be controlled by the combination of D_S and D_C . Figure 16 shows the peak- λ_{PL} contour map of IV-QDs in various D_S and D_C conditions obtained from the data in Figs. 9, 12(a), 14(b), and 15(b). A longer λ_{PL} can be obtained by increasing the D_S at a lower D_C . In contrast, a shorter λ_{PL} can be realized by increasing the D_C at a lower D_S . Consequently, the peak- λ_{PL} of IV-QDs from near-UV to near-IR regions can be easily designed only by the combination of D_S and D_C conditions.

4. Conclusion

In this work, we experimentally studied the group-IV semiconductor-QDs of Si, SiC, and C in a SiO_2 layer fabricated by hot-ion implantation at T and post N_2 annealing

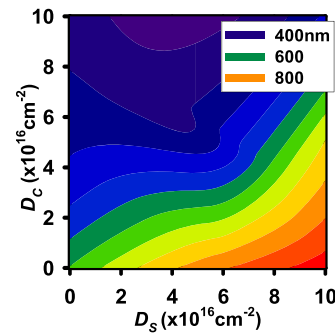


Fig. 16. (Color online) Peak- λ_{PL} contour map in various D_S and D_C conditions for designing peak emission wavelength of IV-QDs. This contour map of peak- λ_{PL} was obtained using the data from Figs. 9, 12, and 14. A longer λ_{PL} can be obtained by increasing D_S at a lower D_C . In contrast, a shorter λ_{PL} can be realized by increasing D_C at a lower D_S .

at a T_N of $1000 \text{ }^\circ\text{C}$. Si- and C-QDs, in addition to SiC-QDs, can be successfully formed around the middle of the SiO_2 layer with a relatively higher dopant concentration using HAADF-STEM. CSTEM also shows clear lattice spots in some areas of IV-QDs, as confirmed by HAADF-STEM, which indicates that some areas of IV-QDs are crystallized. The IV-QD diameter Φ varied from approximately 2–4 nm, and the statistical distribution of Φ can be explained by the Gaussian function. The QD surface-density N was approximately $2 \times 10^{12} \text{ cm}^{-2}$. The Φ and N of the SiC-QDs were affected by T .

The UV-Raman data for the Si- and C-QDs show that the QD crystal quality was improved after N_2 annealing because the c-Si Raman intensity of the Si-QDs and the G-band intensity of the C-QDs increased. Moreover, the UV-Raman spectra of the SiC-QDs strongly depend on D_S/D_C , and the Raman intensities of the TO and D-bands increase with decreasing D_S even at a fixed D_C , which suggests that the SiC and graphite formations in SiC-QDs increase at low D_S conditions.

We experimentally demonstrated strong PL emissions in a wide range of E_{PH} (peak- λ_{PL}) values, even from Si- and C-QDs, in addition to SiC-QDs. The PL spectrum line shape strongly depends on the type of IV-QDs, and different E_{PH} (peak- λ_{PL}) values can be obtained from 1.56 eV (800 nm) of Si-QDs to 3.3 eV (380 nm) of C-QDs, simply by changing the type of IV-QDs. Moreover, the PL intensity of the IV-QDs drastically increased after a short N_2 annealing, which indicates that post N_2 annealing is a key process for realizing strong PL intensity by improving the crystal quality of the IV-QDs. The PL intensity of the SiC-dots in the Si layer gradually decreased after a long N_2 annealing, which could be attributable to the decomposition of the Si-C bond during long high-temperature annealing. However, the PL intensity of the IV-QDs in SiO_2 layer continues to increase with increasing t_N , which is advantageous for the thermal stability of IV-QDs. We experimentally confirmed that the PL emission efficiency of Si-QDs is equal to that of SiC-QDs, but the PL emission efficiency of C-QDs was approximately 1/4 that of Si- and SiC-QDs. In addition, for Si-QDs with an average Φ of 2.4 nm, the E_{PH} of 1.56 eV can be explained by the quantum E_G -expansion via the Φ reduction. In addition, the HWTM of the PL spectrum of Si-QDs is also attributable to the Si-QD Φ variation effect on quantum E_G -expansion in

this study. It was also found that the I_{PL} and E_{PH} of Si- and C-QDs depend on the ion doses.

The PL spectrum of SiC-QDs also depends on the D_S/D_C even at a fixed D_C , and the I_{PL} and E_{PH} increase with decreasing D_S/D_C . These results suggest that the optimum D_S/D_C condition exists to realize higher PL intensity and to design a desired E_{PH} (peak- λ_{PL}). Moreover, the PL spectrum of SiC-QDs can be also explained by five PL components of different cubic/hexagonal SiC-polytypes and Si-C alloys. With increasing D_S/D_C , the PL component of 3C-SiC is almost constant, but the hexagonal-SiC component decreases.

Consequently, this work showed that the peak- λ_{PL} of IV-QDs can be controlled using only two parameters, D_S and D_C . A longer λ_{PL} can be obtained by increasing D_S at a lower D_C , and a shorter λ_{PL} can be realized by increasing the D_C at a lower D_S .

In summary, we demonstrated very strong PL emissions from IV-QDs with different λ_{PL} values for near-IR in Si-QDs, the visible range in SiC-QDs, and near-UV in C-QDs, showing that it is easy to design a desired peak- λ_{PL} simply by controlling the combination of ion doses of Si^+ and C^+ that are implanted into the SiO_2 layer.

Acknowledgments

This work was partially supported by a Grant-in-Aid for Scientific Research from the Japan Society for the Promotion of Science (17K06359).

- 1) Z. C. Feng, *SiC Power Materials: Devices and Applications* (Springer, Berlin, 2010).
- 2) J. Fan and P. K. Chu, *Silicon Carbide Nanostructure* (Springer, Berlin, 2014), Chaps. 3–7.
- 3) T. Kimoto and J. A. Cooper, *Fundamentals of Silicon Carbide Technology* (IEEE, Piscataway, NJ, 2014), Chaps. 2, 5.
- 4) T. Kimoto, S. Nakazawa, K. Hashimoto, and H. Matsunami, *Appl. Phys. Lett.* **79**, 2761 (2001).
- 5) K. Adhikari and A. K. Ray, *J. Nanopart. Res.* **14**, 816 (2012).
- 6) S. Kim, J. E. Spanter, and I. P. Herman, *Jpn. J. Appl. Phys.* **39**, 5875 (2000).
- 7) T. V. Torchynska, A. D. Canoa, S. J. Sandoval, M. Dybic, S. Ostapenkoc, and M. Mynbaevad, *Microelectron. J.* **36**, 536 (2005).
- 8) S. Lin, S. Zhang, X. Li, W. Xu, X. Pi, X. Liu, F. Wang, H. Wu, and H. Chen, *J. Phys. Chem. C* **119**, 19772 (2015).
- 9) E. Bekaroglu, M. Topsakal, S. Cahangirov, and S. Ciraci, *Phys. Rev. B* **81**, 075433 (2010).
- 10) G. Wei, W. Qin, G. Wang, J. Sun, J. Lin, R. Kim, D. Zhang, and K. Zheng, *J. Phys. D: Appl. Phys.* **41**, 235102 (2008).
- 11) L. Latu-Roman and M. Ollivier, *Silicon Carbide One-Dimensional Nanostructures* (Wiley, London, 2015).
- 12) J. A. Borders, S. T. Picraux, and W. Beezhold, *Appl. Phys. Lett.* **18**, 509 (1971).
- 13) Y. H. Gao, Z. Zhang, L. S. Liao, and X. M. Bao, *Appl. Phys. Lett.* **66**, 2382 (1995).
- 14) Y. Shimizu et al., *Appl. Phys. Lett.* **98**, 232101 (2011).
- 15) Y. Shimizu, H. Takamizawa, K. Inoue, F. Yano, S. Kudo, A. Nishida, T. Toyama, and Y. Nagai, *Jpn. J. Appl. Phys.* **55**, 026501 (2016).
- 16) T. Mizuno, Y. Omata, R. Kanazawa, Y. Iguchi, S. Nakada, T. Aoki, and T. Sasaki, *Jpn. J. Appl. Phys.* **57**, 04FB03 (2018).
- 17) T. Mizuno, Y. Nagamine, Y. Omata, Y. Suzuki, W. Urayama, T. Aoki, and T. Sameshima, *Jpn. J. Appl. Phys.* **55**, 04EB02 (2016).
- 18) T. Mizuno, Y. Omata, Y. Nagamine, T. Aoki, and T. Sameshima, *Jpn. J. Appl. Phys.* **56**, 04CB03 (2017).
- 19) T. Mizuno, R. Kanazawa, Y. Omata, T. Aoki, and T. Sameshima, *Jpn. J. Appl. Phys.* **58**, SSBJ01 (2019).
- 20) T. Mizuno, M. Yamamoto, T. Aoki, and T. Sameshima, Abstract of IEEE Silicon Nanoelectronics Workshop 2019, 2019 (Kyoto, Japan) (IEEE, Piscataway, NJ), p. 115.
- 21) T. Mizuno, M. Yamamoto, S. Nakada, S. Irie, T. Aoki, and T. Sameshima, *Jpn. J. Appl. Phys.* **58**, 081004 (2019).
- 22) L. Pavesi and D. J. Lockwood, *Silicon Photonics* (Springer, Berlin, 2004).
- 23) S. Saito et al., *Jpn. J. Appl. Phys.* **45**, L679 (2006).
- 24) S. Saito et al., *IEDM Tech. Dig.*, 2008, p. 19.5.
- 25) T. Mizuno, T. Aoki, Y. Nagata, Y. Nakahara, and T. Sameshima, *Jpn. J. Appl. Phys.* **52**, 04CC13 (2013).
- 26) T. Mizuno, Y. Suzuki, Y. Nagamine, Y. Nakahara, Y. Nagata, T. Aoki, and T. Maeda, *Jpn. J. Appl. Phys.* **54**, 04DC02 (2015).
- 27) S. M. Sze and K. K. Ng, *Physics of Semiconductor Devices* (Wiley, New York, 2007), Chap. 1.
- 28) T. Mizuno, R. Kanazawa, T. Aoki, and T. Sameshima, *Jpn. J. Appl. Phys.* **59**, SGGH-02 (2020).
- 29) L. Pavesi and R. Turan, *Silicon Nanocrystal* (Wiley-VCH, Weinheim, 2010).
- 30) H. Li, J. Wu, and Z. M. Wang, *Silicon-based Nanomaterials* (Springer, New York, 2013).
- 31) N. Yang, X. Jiang, and D.-W. Pang, *Carbon Nanoparticles and Nanostructures* (Springer, Berlin, 2016).
- 32) T. Mizuno, R. Kanazawa, K. Yamamoto, K. Murakawa, K. Yoshimizu, M. Tanaka, T. Aoki, and T. Sameshima, Ext. Abstr. Solid State Devices and Materials, 2020, p. 751.
- 33) D. Tsoukalas, C. Tsamis, and P. Normand, *J. Appl. Phys.* **89**, 7809 (2001).
- 34) B. Schultrich, *Tetrahedrally Bonded Amorphous Carbon Films I* (Springer, Berlin, 2017).
- 35) C. Binns, S. H. Bakar, S. Louch, F. Sirotti, H. Cruguel, P. Prieto, S. C. Thornton, and J. D. Bellier, *Appl. Surf. Sci.* **226**, 249 (2003).
- 36) K. Sato, R. Saito, Y. Oyama, J. Jiang, L. G. Cançado, M. A. Pimenta, A. Jorio, G. G. Samsonidze, G. Dresselhaus, and M. S. Dresselhaus, *Chem. Phys. Lett.* **427**, 117 (2006).